

Microwave ISM Emission in the Green Bank Galactic Plane Survey: Evidence for Spinning Dust

Douglas P. Finkbeiner¹

Princeton University, Department of Astrophysics, Peyton Hall, Princeton, NJ 08544

Glen I. Langston, Anthony H. Minter

National Radio Astronomy Observatory, P.O. Box 2, Green Bank, WV 24944

ABSTRACT

We observe significant dust-correlated emission outside of H II regions in the Green Bank Galactic Plane Survey ($-4 < b < 4^\circ$) at 8.35 and 14.35 GHz. The rising spectral slope rules out synchrotron and free-free emission as majority constituents at 14 GHz, and the amplitude is at least 500 times higher than expected thermal dust emission. When combined with the Rhodes (2.326 GHz), and *WMAP* (23-94 GHz) data it is possible to fit dust-correlated emission at 2.3–94 GHz with only soft synchrotron, free-free, thermal dust, and an additional dust-correlated component similar to Draine & Lazarian spinning dust. The rising component generally dominates free-free and synchrotron for $\nu \gtrsim 14$ GHz and is overwhelmed by thermal dust at $\nu \gtrsim 60$ GHz. The current data fulfill most of the criteria laid out by Finkbeiner *et al.* (2002) for detection of spinning dust.

Subject headings: diffuse radiation — dust, extinction — ISM: clouds — radiation mechanisms: thermal — radio continuum: ISM

1. INTRODUCTION

The statistical detection of anomalous dust-correlated emission, far brighter than expected thermal dust emission at $\sim 10 - 30$ GHz, has been well established (*COBE*, Kogut *et al.* 1996; Saskatoon, de Oliveira-Costa *et al.* 1997; OVRO, Leitch *et al.* 1997; 19 GHz survey, de Oliveira-Costa *et al.* 1998; Tenerife, de Oliveira-Costa *et al.* 1999). There has

¹Hubble Fellow, Henry Norris Russell Fellow

also been a convincing detection of this component in the dark cloud LDN1622 (Lynds 1962), and a detection of a rising spectrum in the diffuse H II region LPH 201.663+1.643 (Lockman *et al.* 1996) using the Green Bank 140 foot telescope, but the interpretation as spinning dust is tentative (Finkbeiner *et al.* 2002). In most cases, free-free emission from ionized gas is ruled out as the source, either by a significantly rising spectrum or by morphological comparison with H α maps. This anomalous dust-correlated emission has been called the “mystery component” or “Foreground X” (de Oliveira-Costa *et al.* 2002) to avoid premature interpretation of the signal. One possible explanation for this emission is electric dipole emission from rapidly ($\sim 1.5 \times 10^{10} \text{ s}^{-1}$) rotating small dust grains, known as “spinning dust” (Draine & Lazarian 1998). Another possibility is magnetic dipole emission due to thermal fluctuations in the magnetization of magnetic grains (Draine & Lazarian 1999). Henceforth, we follow de Oliveira-Costa and refer to “Foreground X,” keeping these two mechanisms in mind as the most likely. Either mechanism might be the dominant source of dust-correlated microwave emission in the diffuse ISM at $\sim 15 - 60$ GHz, overwhelmed by free-free and synchrotron emission at lower frequencies and nonmagnetic thermal dust emission at higher frequencies.

Even though Foreground X could be ubiquitous, severe limitations in previous data sets have prevented a convincing detection over a large solid angle. Surveys such as the 19.2 GHz survey (Cottingham 1987, Boughn *et al.* 1992) and the Tenerife (Gutiérrez *et al.* 2000) survey have such large beams (3° and 5° FWHM respectively) that any diffuse ISM emission in the plane is confused with H II regions, and even when it can be detected by spectral slope (as in the Tenerife data at 10 and 15 GHz) there are relatively few independent pixels in the data showing the rising emission. Other experiments such as *COBE* DMR (7° FWHM) observed at higher frequencies where the spinning dust spectrum is expected to roll off, and cannot be separated from free-free by spectral slope, or spatial resolution. This has made it extremely difficult to argue for an unambiguous detection.

Recently, the *Wilkinson Microwave Anisotropy Probe* (*WMAP*; Bennett *et al.* 2003a) has produced high-sensitivity full-sky maps at 23, 33, 41, 61, & 94 GHz from its first year of data². The main purpose of the mission is to determine cosmological parameters from CMB anisotropy, and this purpose has already been largely fulfilled (Hinshaw *et al.* 2003a, Spergel *et al.* 2003). In addition, the *WMAP* data provide full-sky maps of Milky Way emission in a frequency domain seldom explored before. To interpret this new foreground information, the *WMAP* team performed a Maximum Entropy Method (MEM) analysis as well as more conventional template fitting, and found that the Foreground X is not necessary

²<http://lambda.gsfc.nasa.gov>

to fit the *WMAP* data, instead relying on a hard synchrotron component ($T_b \sim \nu^\beta$ with $\beta \sim -2.5$, typical of supernova remnants) that is strongly correlated with dust (Bennett *et al.* 2003b). The spectrum of this hard synchrotron component (for $23 \text{ GHz} < \nu < 94 \text{ GHz}$) is inconsistent with the Draine & Lazarian cold neutral medium (CNM) model chosen for comparison, but does not disagree strongly with a warm neutral medium (WNM) model scaled slightly in amplitude. Indeed, Finkbeiner (2004) demonstrates in a companion paper that the *WMAP* data off the plane³ can be fit by the following 4 components: 1) soft synchrotron, as traced by 408 MHz (Haslam *et al.* 1982); 2) free-free, as traced by H α emission in three recent surveys (VTSS, Dennison *et al.* 1998; SHASSA, Gaustad *et al.* 2001; WHAM, Haffner *et al.* 2003) as presented by Finkbeiner (2003) plus an enhancement from hot gas within 30° of the Galactic center; 3) Rayleigh-Jeans thermal (vibrational) dust emission as predicted by Finkbeiner, Davis, & Schlegel (1999; hereafter FDS), and 4) a Foreground X template constructed from the FDS dust map times dust temperature squared. The spectral shape of each of the four components is not free to vary with position on the sky, as it is in the *WMAP* MEM analysis, yet the fit is superb. The spectrum derived for Foreground X can be explained by a superposition of Draine & Lazarian spinning dust models, but could also be explained as hard synchrotron highly correlated with dust.

Lagache (2003) has correlated the *WMAP* data with H I maps and found evidence of microwave emission in excess of that expected for synchrotron, free-free, and thermal dust. Banday *et al.* (2003) also address this excess in a new analysis of the *COBE* data and compare to the *WMAP* findings. Recent measurements of the Helix planetary nebula at $26 - 36 \text{ GHz}$ with the Cosmic Background Imager also show a factor of 3 excess over the flux expected in the absence of Foreground X (Casassus *et al.* 2004). Finally, de Oliveira-Costa *et al.* (2004) cross-correlate the *WMAP* MEM synchrotron template (Bennett *et al.* 2003b) with Tenerife data at 10 and 15 GHz, finding the correlation spectrum departs from the expected synchrotron shape by a factor of ~ 10 at 10 GHz. Unfortunately, all of these investigations have some shortcomings: none of the *WMAP*-based analyses have the power to rule out hard synchrotron as the Foreground X component, because at least some spinning dust models are degenerate with hard synchrotron over the frequencies observed ($\nu > 23 \text{ GHz}$), leaving the interpretation of *WMAP* ambiguous. A rising spectrum observed at lower frequencies, seen by de Oliveira-Costa *et al.* (2004), is stronger evidence, but the Tenerife data have a 5° FWHM resolution. Fortunately, higher resolution data at appropriate frequencies do exist.

The Green Bank Galactic Plane Survey (Langston *et al.* 2000) at 8.35 and 14.35 GHz

³where H α extinction is less than 2 mag according to the Schlegel *et al.* (1998) dust map

provides key evidence in favor of Foreground X, even though it was designed to detect transient point sources in the Galactic plane ($|b| < 5^\circ$), not to examine the diffuse ISM. The scan pattern is simpler than would be desired for a diffuse ISM experiment, and in the original analysis the data stream was median filtered on a short timescale to reveal the point sources. However, the survey has the requisite resolution, sensitivity, and frequency coverage to make a highly significant detection of Foreground X. After careful reprocessing of the raw survey data, we have been able to produce images of this anomalous emission on a large angular scale and demonstrate that it is consistent with Draine & Lazarian spinning dust, ruling out hard synchrotron as a majority component at 14 GHz and $|b| < 2^\circ$.

In this paper, we compare Foreground X to spinning dust because of theoretical bias (we know the small grains are there, and they have to spin and radiate at some level) keeping in mind that alternative interpretations, such as magnetic dipole emission, are possible.

In §2 we briefly describe the survey data. Section 3 describes the processing steps taken to produce maps of each “segment” of sky. Results based only on Green Bank data, using the full resolution ($11.2'$) available, are presented in §4. Additional data from Rhodes and *WMAP* (smoothed to 1° FWHM) are analyzed in §5, and conclusions stated in §6.

2. THE DATA

The Green Bank Earth Station (GBES) is a 13.7m dish equipped to communicate with satellites via two receivers centered at 8.35 (X-band) and 14.35 GHz (Ku-band). These receivers view a common beam center on the sky (to within $1/8$ beam) through a dichroic element, allowing simultaneous observation at two frequencies. This simultaneity is advantageous for both satellite communication and transient source surveys, but is also convenient for our purposes. The telescope resolution for point sources is $9.7 \pm 0.1'$ at 8.35 GHz and $6.6 \pm 0.2'$ at 14.35 GHz. After convolving the data samples on to a grid, the effective resolution is $11.2'$ at 8.35 GHz and $8.0'$ at 14.35 GHz. Further details are given in Langston *et al.* (2000).

The scan strategy is to raster the telescope through $-5 < b < 5^\circ$ along a line of (nearly) constant Galactic longitude, sampling total power (both circular polarizations) in a 500 MHz bandwidth 9 times per second (every $2.4'$) along the scan. Successive scans are spaced $5'$ apart, Nyquist sampling the sky at X-band but not at Ku-band. Data are taken in “segments” of 180 scans, covering a patch of $10^\circ \times 15^\circ$ on the sky. The segments are centered on integer multiples of 15° Galactic longitude.

In order to find transient sources, all segments centered on $0 < l < 270^\circ$ were observed

many times and compared. There are four complete surveys (GPA, GPB, GPC, and GPD) each of which nominally consists of 4 epochs a few days apart. Sometimes a given segment is observed several times within one epoch to compensate for bad weather. For the current project we use only GPA, which provides up to 5 observations of each segment, though in practice we choose to use the best three.

3. PROCESSING STEPS

3.1. Segment maps

The processing begins with the gpa-*raw.fit files on Glen Langston’s website⁴. These files contain the time-ordered data, merely a set of sky coordinates (l, b) and measurements in X and Ku band, as well as uncertainties. If the two bands had the same beam on the sky, it would be possible to compare them directly, but because the X-band beam is significantly larger than the Ku-band beam, it is necessary to make a map and smooth the Ku-band beam before comparison.

Each set of 180 scans (covering $10^\circ \times 15^\circ$) constitute a “segment.” Because the scans are not exactly on great circles, the data are mapped to an intermediate scan#- b map, the (n, b) grid, to facilitate Fourier destriping. The instrumental beam is very well sampled in the scan direction (samples every $2.4'$) so linear interpolation in b is sufficient to map to the (n, b) grid. The image is significantly padded in the b direction and Fourier transformed, revealing significant power near the k_b axis outside the band limit, representing stripes in the scan direction. This power is subtracted, and the inverse Fourier transform produces a somewhat cleaner (n, b) map.

After destriping, the data are interpolated along rows of constant b from (n, b) to (l, b) , a Cartesian grid with $2.4'$ pixels. Again a simple linear interpolation is used, because the X-band map is sampled well in this direction, and the Ku-band map, though not quite well sampled, is noisy enough that linear interpolation does not compromise the data, especially considering the subsequent smoothing.

Segments centered on $l = 0, 15, 30, 45$ provide the strongest signal for the current work. We shall refer to these, and other, segments by their central longitude hereafter; all segments center on Galactic latitude zero. Segment -10 is observed at low elevation and suffers from troublesome artifacts due to significant ground pick-up coming through the side-lobes of the

⁴<http://www.gb.nrao.edu/~glangsto/gpa>

antenna. This raises the system temperature resulting in “curved” features in the (l, b) maps which are at a constant elevation above the horizon. These artifacts are understood and are not a problem for other parts of the sky. Segment 60 has weak dust signal and poor weather. Segment 75 is dominated by free-free from a beautiful H II region in Cygnus, but shows little diffuse ISM, and remaining segments in the outer Galaxy show no significant ISM emission. Segment 0 is dominated by free-free, but is included for completeness. Therefore, the results in this paper are derived exclusively from segments 15, 30, and 45.

3.2. Sky subtraction

The total antenna temperature (including system and sky contributions) for these observations is 68 K at X-band and 83 K at Ku-band (sum of both polarizations). The sky contribution to each sample i is $T_{sky,i} = T_0 + T_{sky} \sec z_i$, where z_i is the zenith angle of each sample i , and T_0, T_{sky} are constants fit for each segment. This model is adequate in most cases, but in cases where T_0 or T_{sky} vary during the observation of one segment, a roughly quadratic error can be introduced into the maps, and because X and Ku-band are observed at the same time, the resulting artifacts will be highly correlated. Concerns about this prompted us to re-reduce the data with a more “brute force” approach of fitting a quadratic function of b (with 3σ outlier rejection) to each scan off the plane ($|b| > 2^\circ$) and subtracting the fit. The resulting maps for segments 0,15,30, and 45 are shown in Figure (1-4)a (X-band) and (1-4)b (Ku-band). Note that the result of such fitting is to suppress any extended emission at $|b| > 2$ but such emission is negligible compared to emission in the plane anyway. Bright point sources such as W40 (Segment 30) are preserved by outlier rejection in the baseline fit. Results in this study use this quadratic sky subtraction because it is less susceptible to systematic errors, but the results do not depend significantly on this choice.

3.3. H II region mask

The total emission in the Galactic plane is dominated by a few bright H II regions and supernova remnants. It is desirable to mask these out using independent data, such as the *IRAS* 60/100 μ m flux ratio (Beichman *et al.* 1988). This ratio is approximately 0.2 – 0.3 in the diffuse ISM, and exceeds ~ 0.4 in H II regions. A cut of 0.4 is taken, and grown by 2 pixels in all directions. This mask is shown in outline in Figure 1d. Results are not very sensitive to this choice.

4. Rising spectrum at 8 & 14 GHz

The Green Bank data exhibit a rising intensity from 8 to 14 GHz that cannot be explained by free-free, synchrotron, or thermal (vibrational) dust emission. Data for segments 0, 15, 30, and 45 are shown in Figures 1-4 respectively. In each case, the X and Ku-band images are shown, as well as two superpositions of the X and Ku-band data: one that cancels free-free [$T_K - (14.35/8.35)^{-2.1}T_X$] and another that cancels the ISM in the Galactic plane outside of the *IRAS*-based H II mask. Relative calibration between X and Ku-band is evidently good to better than $\sim 10\%$ or the H II regions would not be canceled by the first superposition so nicely. Note that segment 0 (Figure 1) is dominated by free-free emission and difficult to interpret, but is included for completeness.

A simple test reveals that the X and Ku-band data are consistent with spinning dust models and not with free-free or synchrotron emission. We plot the free-free subtracted [$T_{Ku} - (14.35/8.35)^{-2.1}T_X$] superposition of the two bands vs. dust column (expressed as 100 μ m optical depth, $\tau_{100\mu} = 266 \times E(B - V)$ from Schlegel, Finkbeiner & Davis 1998; hereafter SFD) in Figure 5 and find a strong positive correlation for segments 15, 30, and 45. Of course, a substantial amount of spinning dust would be canceled in this superposition, but an indirect comparison to the 5 Draine & Lazarian (1998) models is possible by computing the same superposition for each model. The Draine & Lazarian models are expressed as emissivity per H column density, so we convert $N(H)$ to 100 μ m optical depth using 2.13×10^{24} H cm $^{-2}$ = unit $\tau_{100\mu}$ to obtain a slope for each model⁵. One symbol is plotted for each 12' \times 12' independent region in each of the four segments; the vast majority fall among the 5 spinning dust model lines. A region dominated by free-free would fall on the horizontal line; any emission with a slope steeper than $\beta = -2.1$ (such as hard synchrotron) would fall below the line. A few such regions appear, such as SNR 3C392 in segment 30, but in general most pixels outside the H II mask appear to be consistent with the spinning dust interpretation of Foreground X, and inconsistent with free-free or synchrotron emission alone.

5. Green Bank and *WMAP*

The previous section provided support for the spinning dust hypothesis, by demonstrating a rising spectrum in the Green Bank data from 8 to 14 GHz. By combining those data with the Rhodes survey (2.326 GHz; see Jonas *et al.* 1998) and *WMAP* (23 – 94 GHz) we

⁵This factor assumes a mean dust temperature of 18.175K obtained by SFD98 and a ratio of 8×10^{21} H cm $^{-2}$ per magnitude $E(B - V)$ derived by SFD98 by comparing 21cm H I emission with dust FIR emission. This latter factor differs from the value of 5.8×10^{21} H cm $^{-2}$ reported by Bohlin *et al.* 1978

can now produce a spectrum of dust-correlated emission from 2.3 – 94 GHz.

5.1. Choice of dust template

By cross-correlating the data in each band against a dust template (such as SFD) and measuring the correlation slope, we can obtain the desired information without being confused by sometimes poorly determined zero points of the various data sets. As a template we could use SFD dust (as in the previous section) or dust times some power of dust temperature (as in Finkbeiner 2004), but for the present analysis we prefer the *WMAP* 94 GHz map⁶. This map is dominated by thermal dust emission on the Rayleigh-Jeans tail, where temperature dependence is weak, so it is a good tracer of total dust column density. This way the errors in the SFD dust temperature correction at low Galactic latitude do not propagate into the analysis. All three templates have been used in the following analysis with nearly identical results, but the 94 GHz map produces tighter scatter and small error bars.

5.2. Correlation slopes

Scatter plots for each of 9 channels (0.408, 2.326, 8.35, 14.35, 23, 33, 41, 61, 94 GHz) vs. 94 GHz are shown for segment 30 in Figure 6 along with best fit linear regression lines. For this analysis, all maps are smoothed to 1° FWHM and the H II region mask is appropriately enlarged. Dashed lines indicate the 1σ width of the distribution of slopes, *not* the uncertainty in the mean, which is much smaller.

These slopes are then converted to $j_\nu \tau_{100\mu}^{-1}$ for comparison with results obtained in the previous section. Draine & Lazarian models refer to $N(H)$ because they are physical models tied to element abundances relative to H. In practice, the microwave emissivities are compared to dust optical depth (without regard for whether the associated H is molecular, neutral atomic, or ionized) and the models are converted from j_ν/n_H (Jy $\text{cm}^2\text{sr}^{-1}$ H $^{-1}$) to $j_\nu \tau_{100\mu}^{-1}$ (Jy sr^{-1}) with a canonical factor $2.13 \times 10^{24} \text{ H cm}^{-2} = \text{unit } \tau_{100\mu}$. In the case of the 94 GHz template, a conversion factor of 34.6 mK⁷ per unit $\tau_{100\mu}$ is applied, corresponding to 0.13 mK per mag $E(B - V)$ is applied. This conversion factor can be fit empirically from

⁶The effective central frequency for *WMAP* W-band is 93.1 GHz for free-free and 94.3 GHz for dust. Because thermal dust is the dominant Galactic emission in W-band, we refer to it as the “94 GHz” band throughout.

⁷antenna temperature, not thermodynamic ΔT

the SFD maps and *WMAP* 94 GHz data, or derived from a comparison of the FIRAS-based Finkbeiner *et al.* (1999) 94 GHz prediction and the SFD $\tau_{100\mu}$ map for median dust temperature. Correlation slopes are fit for the 4 segments, with segments 15, 30, and 45 showing a pronounced rise from 8 to 14 GHz and requiring some sort of anomalous emission (Figure 7).

As a toy model, a superposition of 0.18 times the Draine & Lazarian molecular cloud model plus 0.5 times the Draine & Lazarian WNM spectrum is used, where the electric dipole moment is increased by a factor of two for the WNM curve. The WNM term is an extrapolation based on the Draine & Lazarian WNM model for two values of the electric dipole moment, and is not a rigorous calculation. This parameterization should not be taken seriously as a physical interpretation of the spectrum; it merely shows that a superposition of reasonable models provides a good fit to the data. Further study will be required to fit these curves in detail with a physical spinning dust model.

5.3. Magnetic Dust

Another emission mechanism that could produce Foreground X is magnetic dust (Draine & Lazarian 1999; DL99). This mechanism has nothing to do with rapid rotation of magnetic dipoles; rather it results from the thermal fluctuations in the grain magnetization, yielding an additional thermal emissivity mechanism. The published DL99 models have a slow roll off above the peak intensity, and this roll off results in high theoretical 61 GHz correlation slopes relative to the *WMAP* data. That is to say, for the measured 61 GHz to be so low, a sharp roll off in the underlying dust spectrum with increasing frequency is required. However, it may be possible to tune the dust magnetic susceptibility function to produce a steep roll off (Draine priv. comm.). We have not explored this parameter space, but simply note that while the published magnetic models appear to be ruled out by the data, a variant of such models may not be ruled out as a majority contribution. Further theoretical work is required before the dominant dust-correlated emission mechanism can be unambiguously identified. What is certain, however, is that it is not hard synchrotron emission alone.

5.4. Limits on Hard Synchrotron

The *WMAP* team (Bennett *et al.* 2003b) claims that hard synchrotron ($\beta = -2.5$) emission from dusty star forming regions is the main contributor to dust-correlated emission at 23 GHz. They arrived at this conclusion without the benefit of any diffuse ISM measure-

ments of the Milky Way between 2.3 and 23 GHz. Now that a rise in the dust spectrum has been observed in the 8 and 14 GHz Green Bank data, it is evident that another emission mechanism is required. By assuming that Foreground X contributes nothing at 8 GHz and rises sharply to 14 GHz (and ignoring all other components such as free-free) one can make the conservative statement that hard synchrotron is less than 2/3 of the 14 GHz intensity, and less than 1/2 at 23 GHz (based on the data in Table 1). Inclusion of free-free or soft synchrotron pushes these limits down further. We therefore conclude that dust-correlated hard synchrotron provides less than 1/2 the intensity in the *WMAP* bands, and possibly much less.

5.5. Calibration check: W40

The arguments in this paper depend most heavily on the spectral rise observed in the 8 and 14 GHz Green Bank maps, and so the calibration of these maps deserves close scrutiny. In order to verify the calibration of the Green Bank data relative to *WMAP* (which has a calibration uncertainty of less than 1%, Hinshaw *et al.* 2003b) we single out the H II region W40 at $(l, b) = 28.8^\circ, 3.5^\circ$, and repeat the above analysis. W40 is an association of at least 6 luminous stars adjacent to a molecular cloud (see Smith *et al.* 1985 for details) and is certainly an inhomogeneous environment. However, at the scale of comparison (1°) it is unresolved. *WMAP* 94 GHz data are again used as a dust template, only all correlation slopes are multiplied by 1.8 (i.e. 94 GHz emission per $\tau_{100\mu}$ is high by that factor here, determined by a fit to the W40 spectrum) to account for the fact that only part of the 94 GHz emission in this H II region is actually thermal dust. The W40 spectrum (Figure 8) appears to be mostly free-free over a wide spectral range, with a small but significant enhancement above 33 GHz. The spinning dust component included is the Draine & Lazarian molecular cloud model times a factor of 0.15, for reference. This is close to the factor of 0.2 suggested by Draine & Lazarian to account for the expected depletion of small grains in molecular clouds. This plot demonstrates that (at least in segment 30) the Green Bank calibration (Langston *et al.* 2000) appears to be compatible with *WMAP* at the 10% level or better. This indicates that the disagreement with the hard synchrotron hypothesis is robust, and does not result from calibration error.

5.6. Sidelobes

Substantial contribution from ground pickup in beam sidelobes is always a potential concern with continuum measurements. At 14 GHz, the brightest regions on the sky are of

order 1 K and the ground is 300K, so ground emission is far more important than reflection of the sky. Such ground emission does appear in the segment centered at $l = -10$, creating an obvious constant elevation pattern, so this segment has been discarded.

Far sidelobes on the sky are not a concern, because the sky baseline for each scan is established by fitting each scan at the ends, $|b| > 2^\circ$, with a quadratic fit. The far (tens of degrees) sidelobes can only produce a very smooth background, and are subtracted by this fit. The only potential contamination comes from the near sidelobes (few degrees off axis) picking up bright objects on the sky.

To verify that near sidelobes are negligible, we scanned the unresolved source Cas A from 8 approach angles, i.e. every by 45° (Figures 10, 11). Artifacts away from the main beam, such as diffraction spikes, are at the few percent level. There is no sign of the second Airy ring, which for a 2m secondary mirror blocking the 13.7m primary would theoretically have an amplitude of 2.4% of the peak and contain 10% of the beam power. Where the scans are slightly off center, diffraction spikes of 3% amplitude can be seen in Fig. 11) near peaks 5 and 6, so the unseen sidelobes are probably less than 1%. This happens because the illumination of the primary is not uniform, but rather rolls off to near zero at the edge of the dish. This apodization suppresses the airy rings, making the amplitude less than the theoretical 2.4%. A 1% amplitude (which seems conservative) implies 4% or less of the total power is scattered into the first Airy ring. Unfortunately, this telescope is no longer in service, so more complete beam maps are impossible to obtain.

It is difficult to imagine sidelobe contamination affecting our correlation slopes by more than a few percent, compared with the factor of 2 discrepancy between the X- and Ku-band data and the Bennett *et al.* synchrotron model.

6. SUMMARY

A previous analysis (Finkbeiner 2004) showed that *WMAP* data off the Galactic plane are consistent with spinning dust emission similar to that proposed by Draine & Lazarian (1998), but agreed with Bennett *et al.* (2003b) that dust-correlated hard synchrotron ($\beta \sim -2.5$) could explain the emission as well. *WMAP* alone cannot differentiate between these two possibilities because the spectral rise predicted for most spinning dust models occurs at lower frequencies ($\nu < 23$ GHz). Because there are no other data of comparable quality at high latitude in the required frequency range, this study makes use of the Green Bank Galactic Plane Survey (8.35, 14.35 GHz) at low latitude ($-4 < b < 4^\circ$), finding a significant spectral rise and ruling out hard synchrotron as a majority contributor at 23 GHz. In light of

this discovery, it is likely that Foreground X dominates hard synchrotron at higher latitudes as well.

Previous attempts to understand microwave foregrounds have missed important features in the data (e.g. by ignoring Foreground X altogether, ignoring effects of dust temperature variation, or failing to identify the free-free Galactic haze seen by Finkbeiner 2004) and we may continue to oversimplify by assuming the same physical mechanism is responsible for all occurrences of Foreground X. In this early phase of the investigation, we have attempted to keep the analysis described herein (fitting correlation slopes as a function of frequency) as straightforward as possible, aiming to demonstrate the existence of Foreground X and motivate further measurements. More sophisticated techniques may be used in the future to refine our understanding of Foreground(s) X, and to derive parameters of physical models for the emission (as in Draine & Lazarian). For example, polarization measurements of clouds such as LDN1622 at 3–10 GHz may constrain spinning dust models (see Lazarian & Draine 2000). The present analysis simply argues strongly for the existence of spinning dust or another component with similar spectral behavior.

We are indebted to Bruce Draine and David Schlegel for encouragement and advice. Carl Heiles and Angelica de Oliveira-Costa provided helpful conversations. This research made use of the NASA Astrophysics Data System (ADS) and the The IDL Astronomy User’s Library at Goddard Space Flight Center⁸. DPF is a Hubble Fellow supported by HST-HF-00129.01-A and by NASA LTSA grant NAG5-12972. The Green Bank Earth Station telescope is located at Green Bank Observatory, operated by the National Radio Astronomy Observatory (NRAO), which is a facility of the National Science Foundation operated under cooperative agreement by Associated Universities, Inc.

⁸<http://idlastro.gsfc.nasa.gov/>

REFERENCES

Banday, A. J., Dickinson, C., Davies, R. D., Davis, R. J., & Górski, K. M. 2003, MNRAS, 345, 897

IRAS Catalogs and Atlases: Explanatory Supplement 1988, eds. Beichman, C. A., Neugebauer, G., Habing, H. J., Clegg, P. E., & Chester, T. J. (Washington, D.C.: U.S. Government Printing Office)

Bennett, C. L., *et al.* 2003a, ApJ, 583, 1

Bennett, C. L., *et al.* 2003b, ApJS, 148, 97

Bohlin, R. C., Savage, B. D., & Drake, J. F 1978, ApJ, 224, 132

Boughn, S. P., Cheng, E. S., Cottingham, D. A., & Fixsen, D. J. 1992, ApJ, 391, L49

Casassus, S., *et al.* 2004, ApJ, 603, 599

Cottingham, D. A. 1987, Ph.D. Thesis, Princeton Univ.

Dennison, B., Simonetti, J. H., & Topasna, G. 1998, Publications of the Astronomical Society of Australia, 15, 147.

de Oliveira-Costa, A., Kogut, A., Devlin, M. J., Netterfield, C. B., Page, L. A., & Wollack, E. J. 1997, ApJ, 482, L17

de Oliveira-Costa, A., Tegmark, M., Page, L., & Boughn, S. 1998, ApJ, 509, L9

de Oliveira-Costa, A., *et al.* 1999, ApJ, 527, L9

de Oliveira-Costa, A., *et al.* 2002, ApJ, 567, 363

de Oliveira-Costa, A., *et al.* 2004, ApJ, 606, L89

Draine, B. T., & Lazarian, A. 1998, ApJ, 508, 157

Draine, B. T., & Lazarian, A. 1999, ApJ, 512, 740

Finkbeiner, D. P., Davis, M., & Schlegel, D. J. 1999, ApJ, 524, 867

Finkbeiner, D. P., Schlegel, D. J., Frank, C., & Heiles, C. 2002, ApJ, 566, 898

Finkbeiner, D. P. 2003, ApJS, 146, 407

Finkbeiner, D. P. 2004, ApJ *in press*, and astro-ph/0311547

Gaustad, J. E., McCullough, P. R., Rosing, W. & Van Buren, D. 2001, PASP, 113, 1326

Gutiérrez, C. M., Rebolo, R., Watson, R. A., Davies, R. D., Jones, A. W., & Lasenby, A. N. 2000, ApJ, 529, 47

Haffner, L. M., Reynolds, R. J., Tufte, S. L., Madsen, G. J., Jaehnig, K. P., & Percival, J. W. 2003, ApJS, 149, 405

Haslam, C. G. T., Stoffel, H., Salter, C. J., & Wilson, W. E. 1982, A&AS, 47, 1

Hinshaw, G., *et al.* 2003a, ApJS, 148, 135

Hinshaw, G., *et al.* 2003b, ApJS, 148, 63

Jonas, J. L., Baart, E. E., & Nicolson, G. D. 1998, MNRAS, 297, 977

Kogut, A., *et al.* 1996, ApJ, 464, L5

Lagache, G. 2003, A&A, 405, 813

Langston, G., Minter, A., D'Addario, L., Eberhardt, K., Koski, K., & Zuber, J. 2000, AJ, 119, 2801

Lazarian, A. & Draine, B. T. 2000, ApJ, 536, L15

Leitch, E. M., Readhead, A. C. S., Pearson, T. J., & Myers, S. T. 1997, ApJ, 486, L23

Lockman, F. J., Pisano, D. J., & Howard, G. J. 1996, ApJ, 472, 173 [LPH]

Lynds, B. T. 1962, ApJS, 7, 1

Page, L., *et al.* 2003, ApJS, 148, 39

Schlegel, D. J., Finkbeiner, D. P., & Davis M. 1998, ApJ, 500, 525 [SFD]

Smith, J., Bentley, A., Castelaz, M., Gehrz, R. D., Grasdalen, G. L., & Hackwell, J. A. 1985 ApJ, 291, 571

Spergel, D. N., *et al.* 2003, ApJS, 148, 175

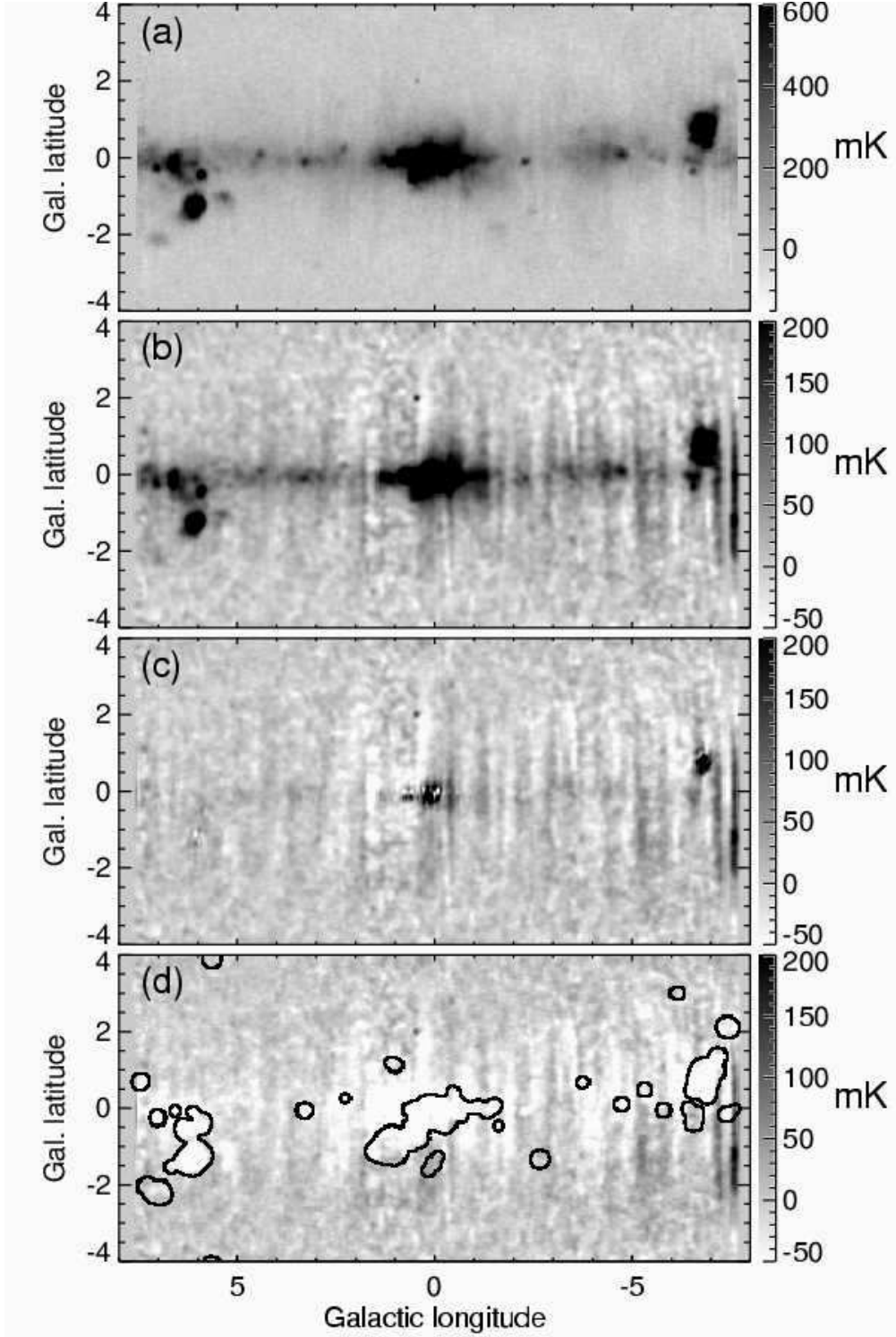


Fig. 1.— GPA segment centered on $l = 0^\circ$: (a) X-band (8.35 GHz) map; (b) Ku-band (14.35 GHz) map, smoothed to X-band beam; (c) free-free subtracted Ku-band map, i.e. $T_{Ku} - (14.35/8.35)^{-2.1}T_X$; and (d) $T_{Ku} - (14.35/8.35)^{-1.2}T_X$ map with outline of H II mask (see §3.3) superposed. The H II regions in (d) are oversubtracted, but the diffuse emission is canceled. This segment exhibits more striping artifacts than the others.

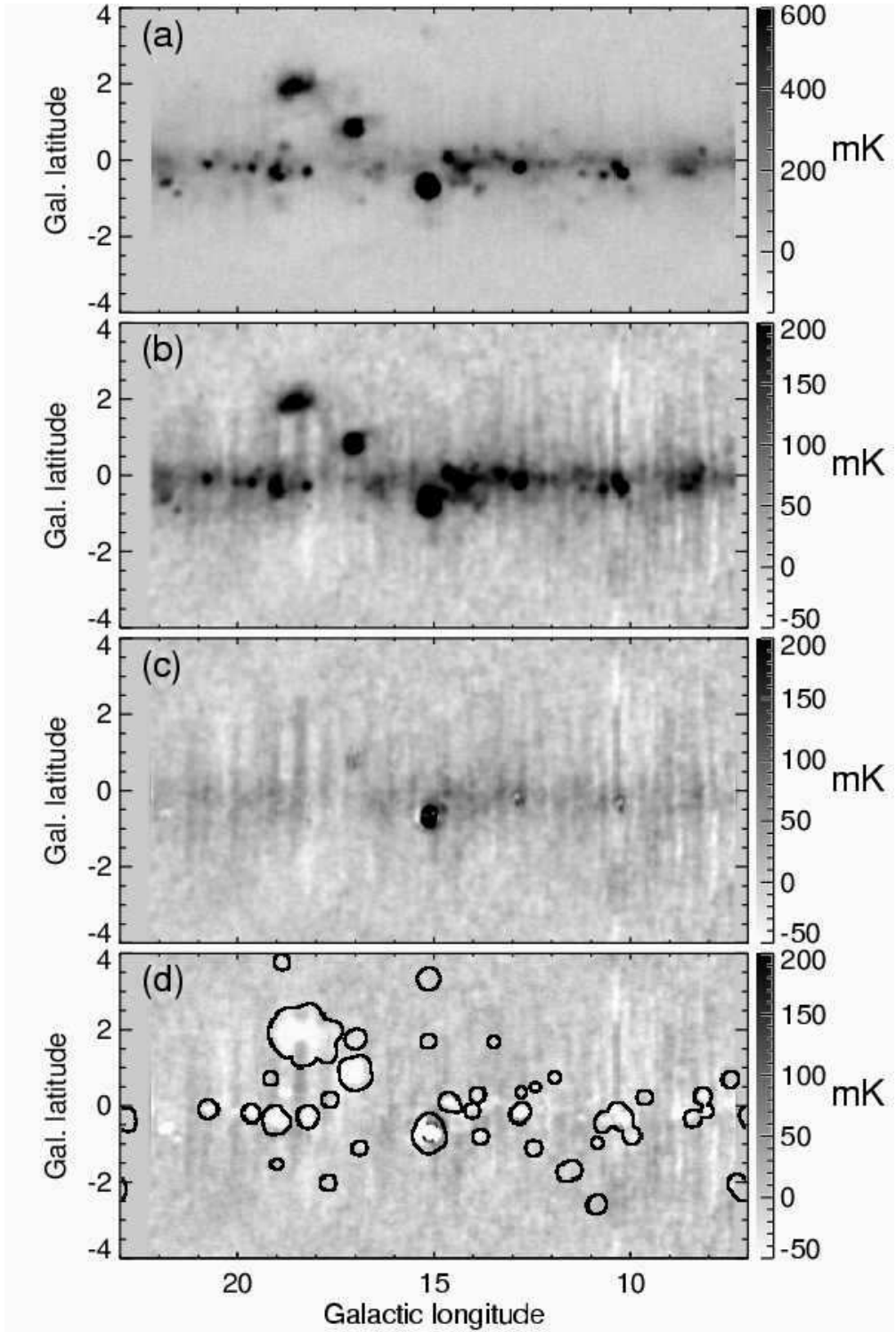


Fig. 2.— GPA segment centered on $l = 15^\circ$, see Figure 1 caption. The subtraction is good in (c) considering that the region around NGC 6618 (l, b) = $15.1^\circ, -0.7^\circ$ is 10 times brighter than the region around NGC 6611 at (l, b) = $17.0^\circ, 0.9^\circ$.

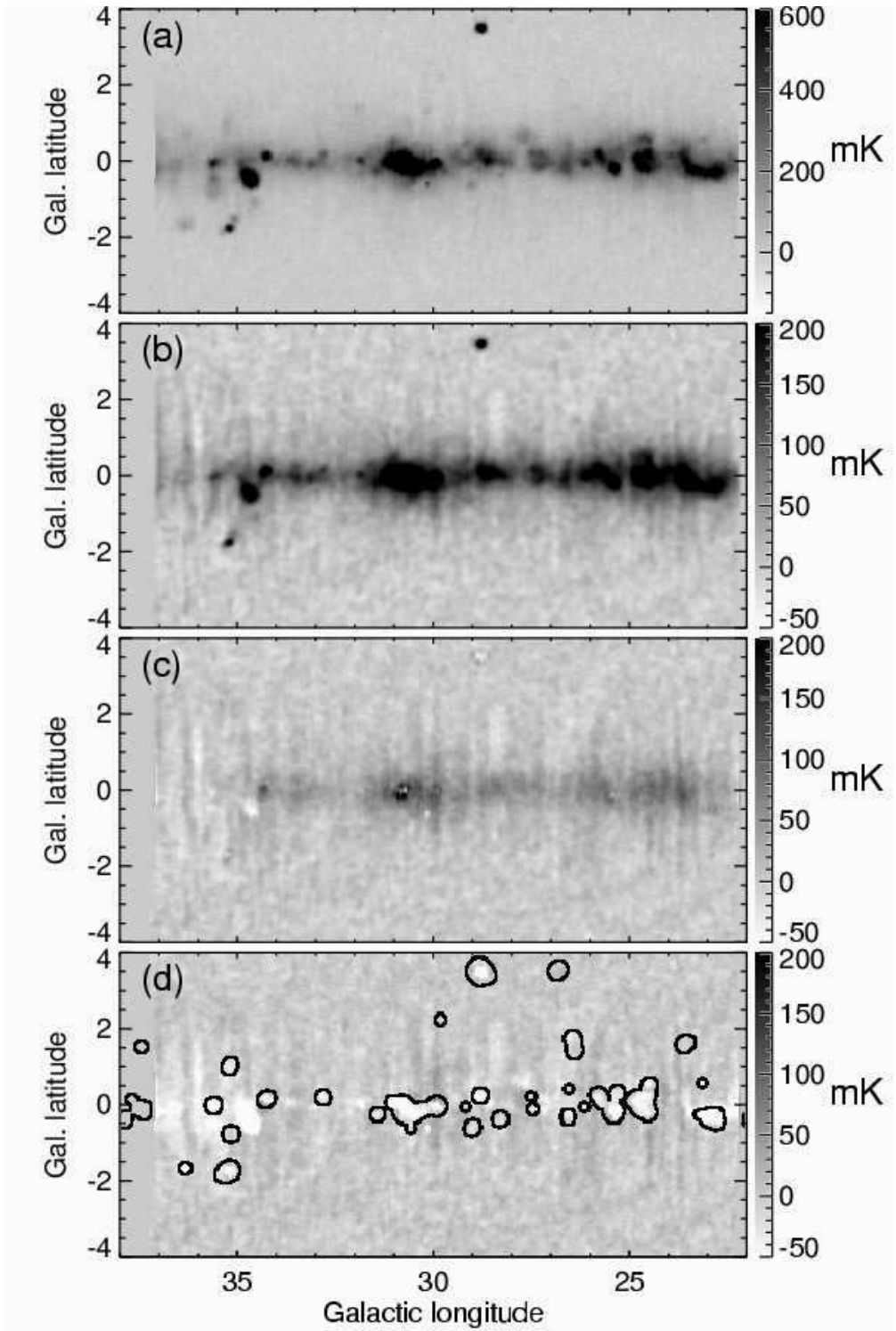


Fig. 3.— GPA segment centered on $l = 30^\circ$; see Figure 1 caption. Oversubtracted regions in this map are dominated by synchrotron emission, such as the SNR 3C392 at $(l, b) = 34.75^\circ, -0.5^\circ$. The W40 complex is visible at $(l, b) = 28.8^\circ, 3.5^\circ$, and is used as a calibration check in §5.5.

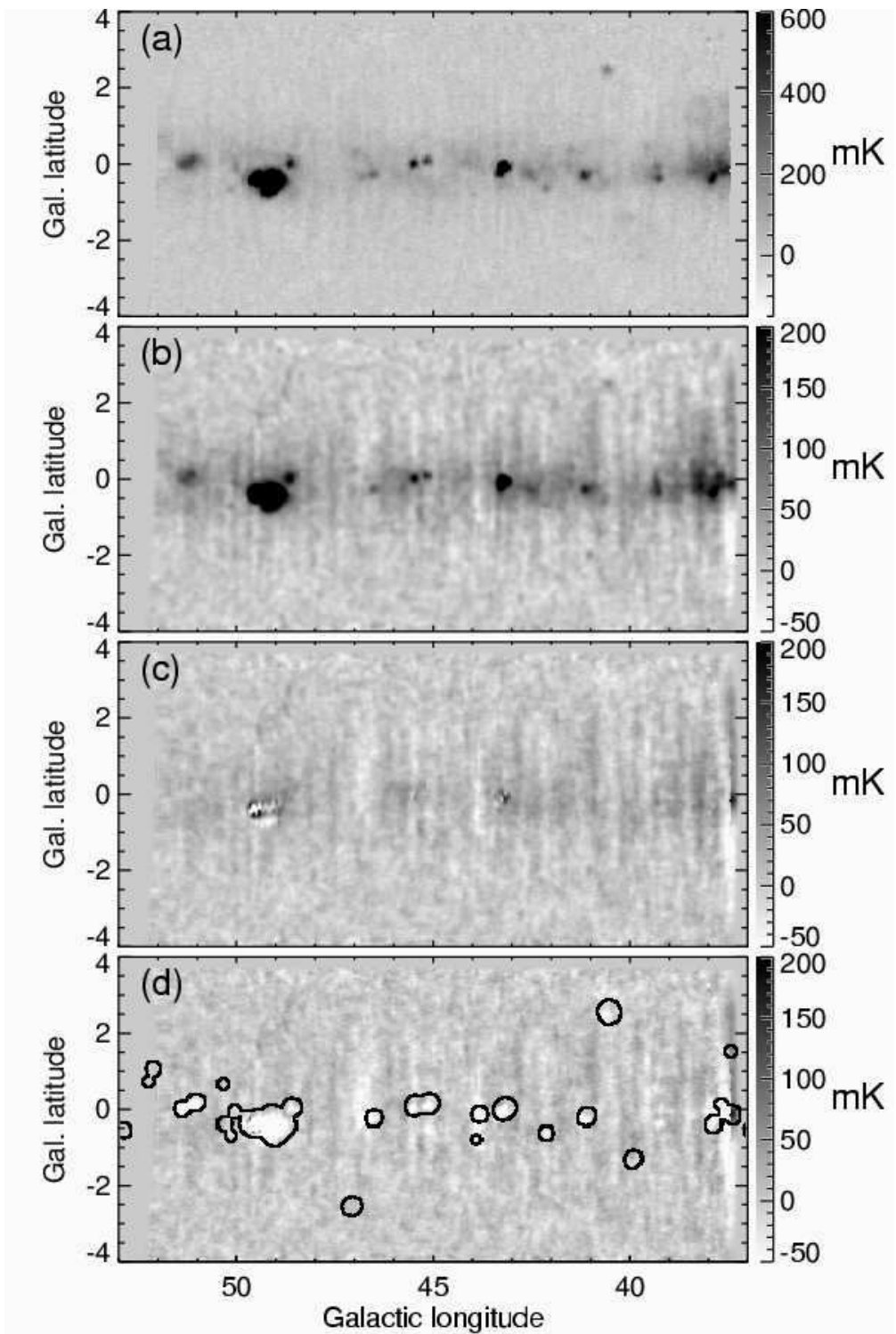


Fig. 4.— GPA segment centered on $l = 45^\circ$; see Figure 1 caption.

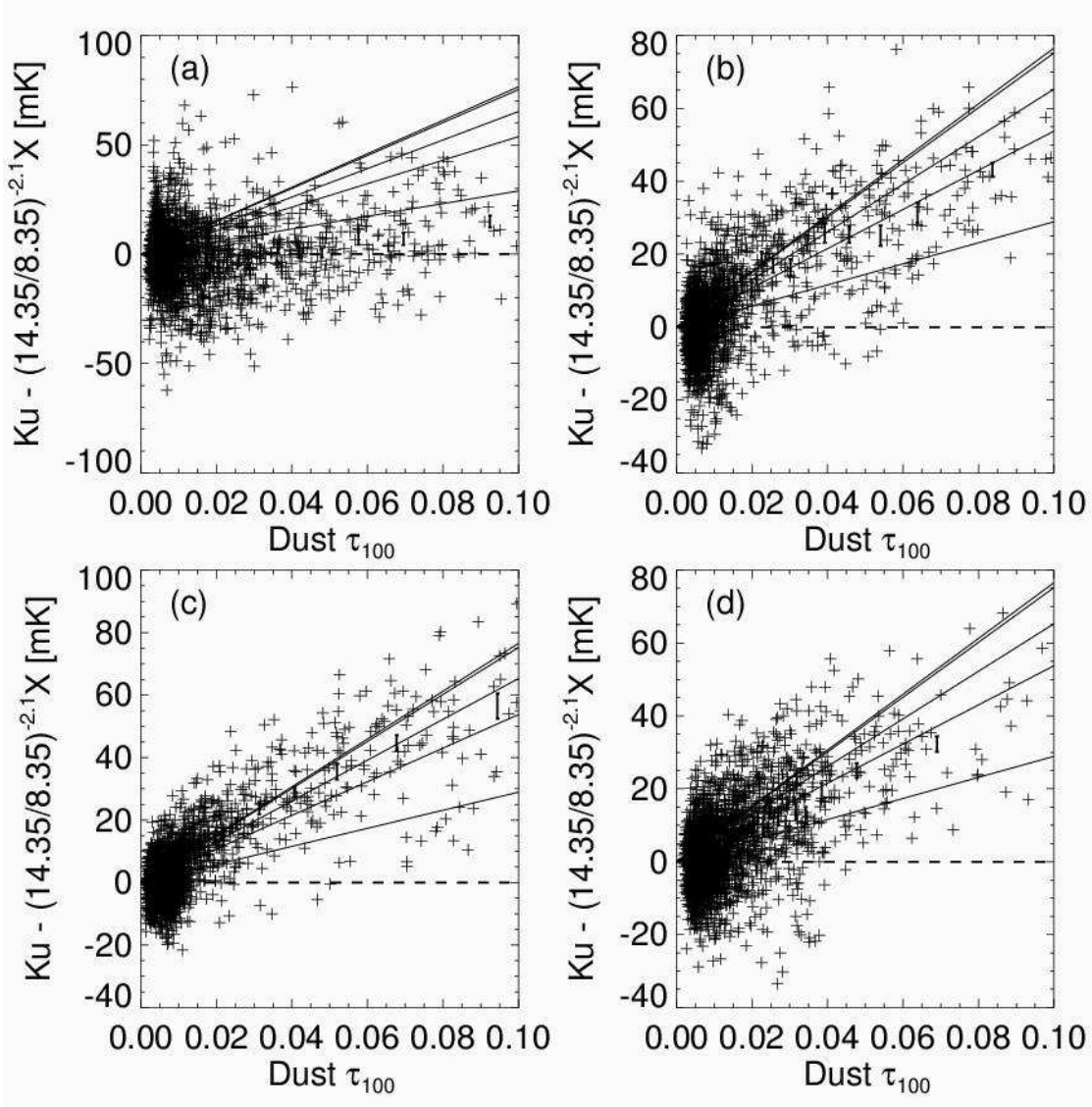


Fig. 5.— Free-free subtracted Ku-band antenna temperature vs. dust optical depth from SFD98 for segments centered at (a) 0° , (b) 15° , (c) 30° , and (d) 45° Galactic longitude. Each symbol represents a $12' \times 12'$ patch of sky (independent beams). Pixels dominated by free-free would fall on the dashed horizontal line and synchrotron would fall below the line in the absence of noise. The solid lines represent 5 Draine & Lazarian (1998) spinning dust models for (from top to bottom) WIM, WNM, CNM, molecular clouds, and dark clouds, respectively. Error bars show 1σ uncertainty of the mean values in bins containing 1/50 of the data points. These error bars do not include an overall calibration uncertainty of 10%. Segments 15, 30, and 45 are consistent with spinning dust models and inconsistent with free-free or synchrotron emission.

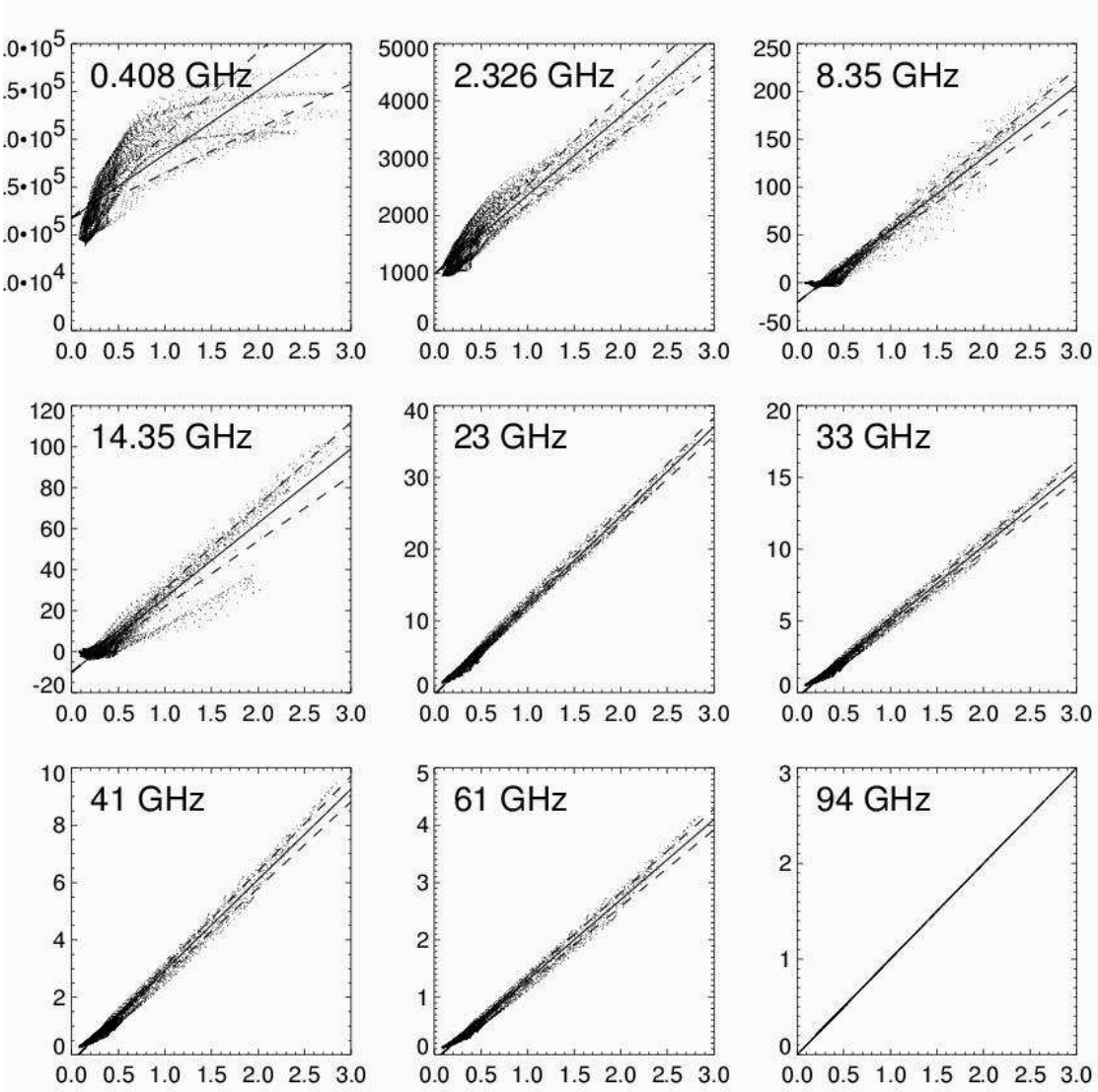


Fig. 6.— Scatter plots for Segment 30. At each of 9 frequencies, antenna temperatures [mK] are plotted vs. the *WMAP* 94 GHz channel, used as a tracer of dust. CMB anisotropy is removed from the 5 *WMAP* bands before plotting. When this plot is made using e.g. SFD98 100 μ m optical depth as a dust tracer, the relative slopes are the same, but the scatter is greater. *WMAP* 94 GHz is dominated by Rayleigh-Jeans dust emission, and is therefore a good proxy for total dust column density. Scatter plots like these were made for all 4 segments, and the correlation slopes are plotted vs. frequency in Figure 7. We discard the Haslam 408 MHz result because the scatter is so non-linear.

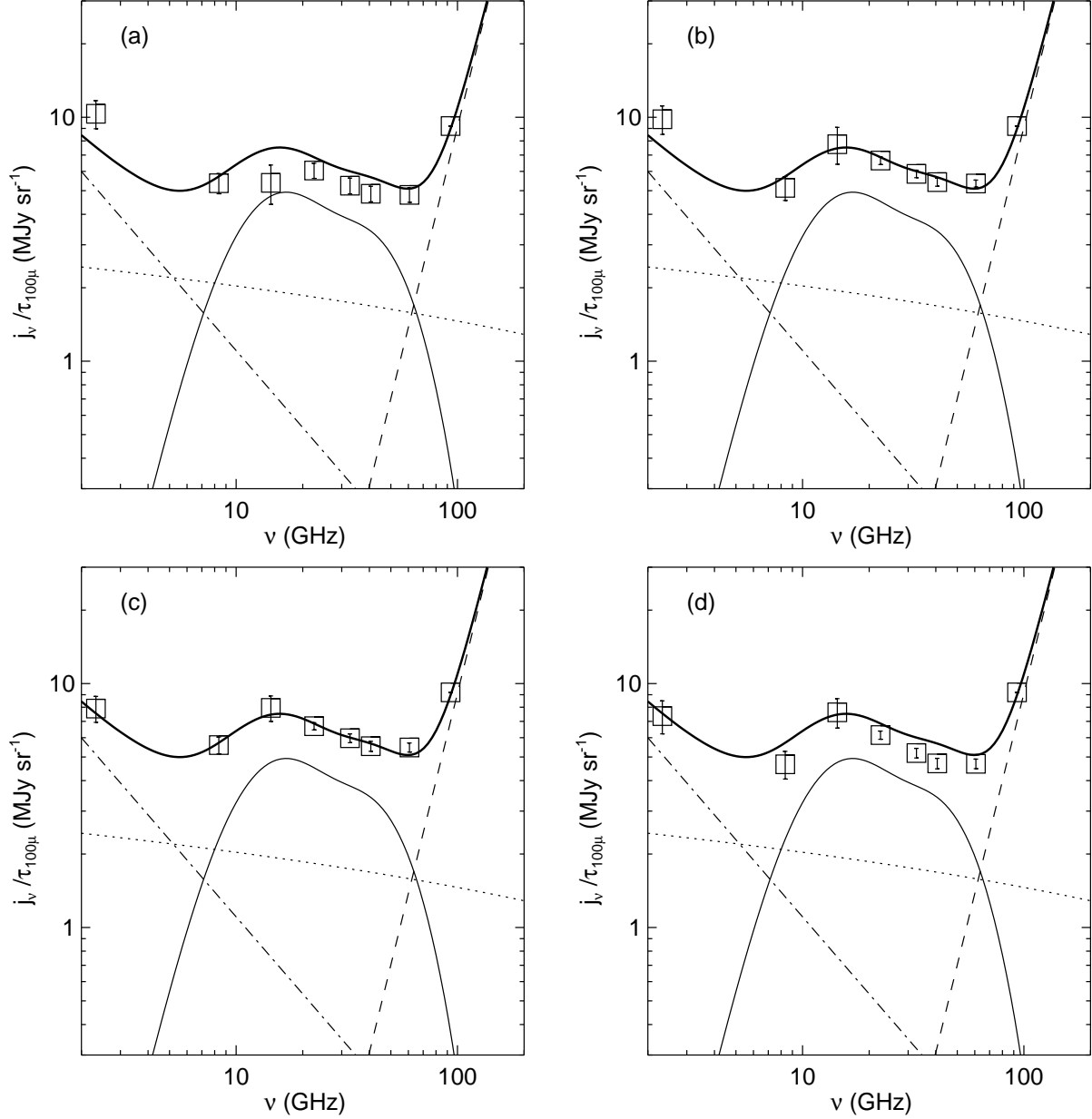


Fig. 7.— Correlation slope spectra for segments (a) 0, (b) 15, (c) 30, and (d) 45. The rise from 8 to 14 GHz cannot be explained with any combination of free-free, synchrotron, and thermal dust. The 94 GHz map is used as a tracer of dust column density, and is placed on this plot using a conversion factor calculated in §5.2. Also shown are free-free (dotted line), synchrotron with index $\alpha = -1.05$ (dash-dot line), thermal dust with Finkbeiner *et al.* (1999) calibration (dashed line), and a mock spinning dust model described in §5.2 (lower solid curve), as well as the sum of these four components (thick solid curve). The same curves are overplotted in each panel to guide the eye, and are not a formal fit to the data.

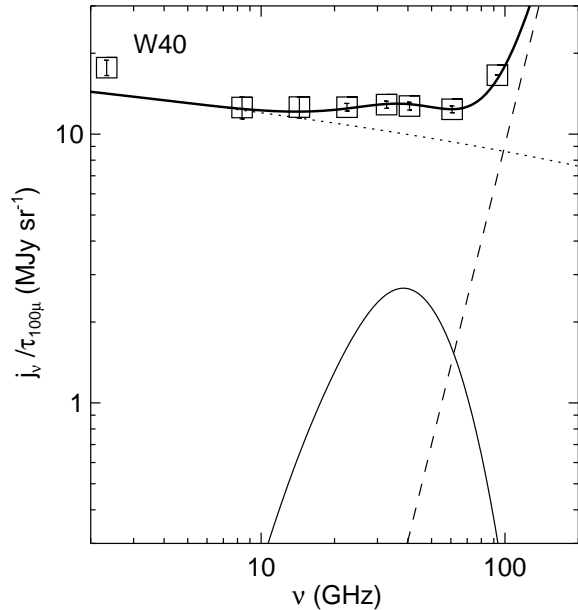


Fig. 8.— Correlation slope spectrum of W40 (also known as LBN90). W40 is an H II region around 6 or more OB stars eating into a large molecular cloud. The dominance of free-free and distance from the Galactic Plane (3.5°) allow this source to be used as a calibration check. The curve through the data points is a sum of free free (*dotted line*), thermal dust (*dashed line*), and 0.15 times the Draine & Lazarian model for molecular cloud spinning dust (*solid line*). This is close to the factor of 0.2 proposed by Draine & Lazarian (1998) to account for the expected depletion of small grains in molecular clouds, but this plot should not be over interpreted; the point is that the Green Bank 8.35 and 14.35 GHz data and the *WMAP* data have a consistent calibration.

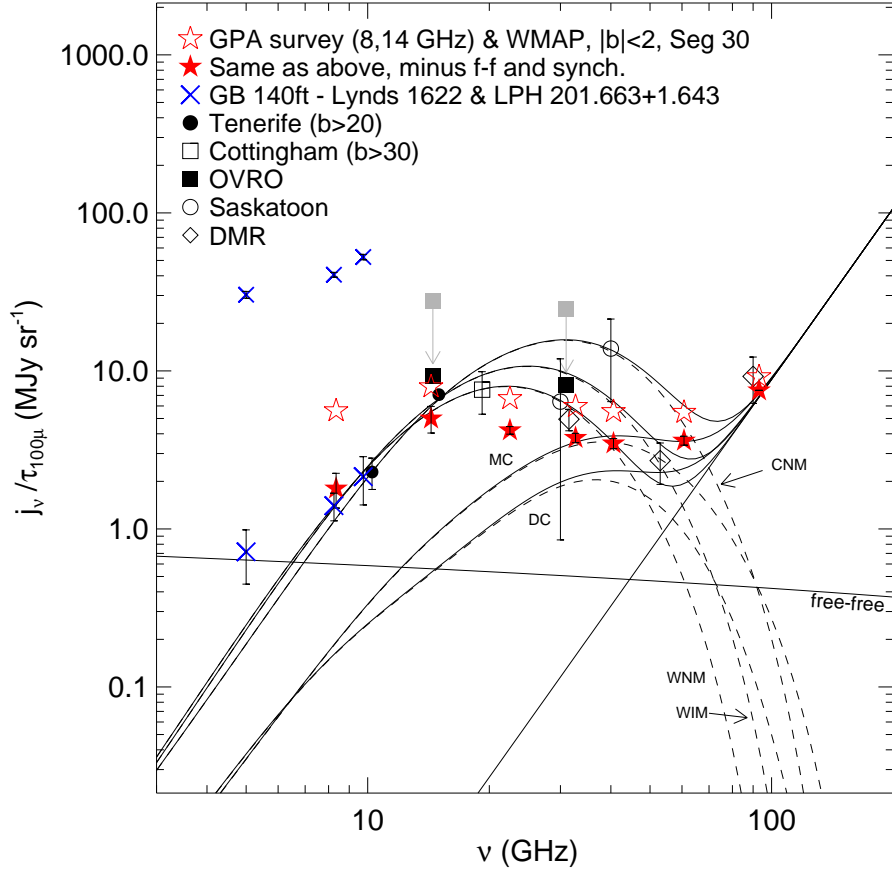


Fig. 9.— Model dust emissivity per $\tau_{100\mu}$ for DC, MC, CNM, WNM, and WIM conditions (as in Draine & Lazarian 1998, Figure 9). Solid thin lines are total emissivity; dashed lines are rotational emission. Gray line is free-free for $\langle n_e n_p \rangle / \langle n_H \rangle = 0.01 \text{ cm}^{-3}$ averaged along the line of sight. Also shown are measurements from the *COBE/DMR* (*open diamonds*) from Finkbeiner *et al.* (1999), similar to Kogut *et al.* (1996); Saskatoon (*open circles*) (de Oliveira-Costa *et al.* 1997); the Cottingham & Boughn 19.2 GHz survey (*open square*) (de Oliveira-Costa *et al.* 1998), OVRO data (*solid squares*) (Leitch *et al.* 1997); Tenerife data (*solid circles*) (de Oliveira-Costa *et al.* 1999); GB140 data for LPH 201.663+1.643 (*upper crosses*) and LDN1622 (*lower crosses*; Finkbeiner *et al.* 2002); and Green Bank / WMAP data for Segment 30 from this study with synchrotron and free free included (*open stars*) and removed (*filled stars*) assuming free-free is $10^{-18} \text{ Jy cm}^2 \text{ sr}^{-1} \text{ H}^{-1}$ at 8.35 GHz and synchrotron is $2.4 \times 10^{-18} \text{ Jy cm}^2 \text{ sr}^{-1} \text{ H}^{-1}$ at 2.326 GHz with $\alpha = -1.05$ as in Figure 7. The OVRO points have been lowered a factor of 3 relative to Draine & Lazarian (1998, Figure 9), because the unusual dust temperature near the NCP caused an underestimate of the H column density along those lines of sight. Given the large range of model curves, most measurements are consistent with some superposition of spinning dust, vibrational dust, and free-free emission.

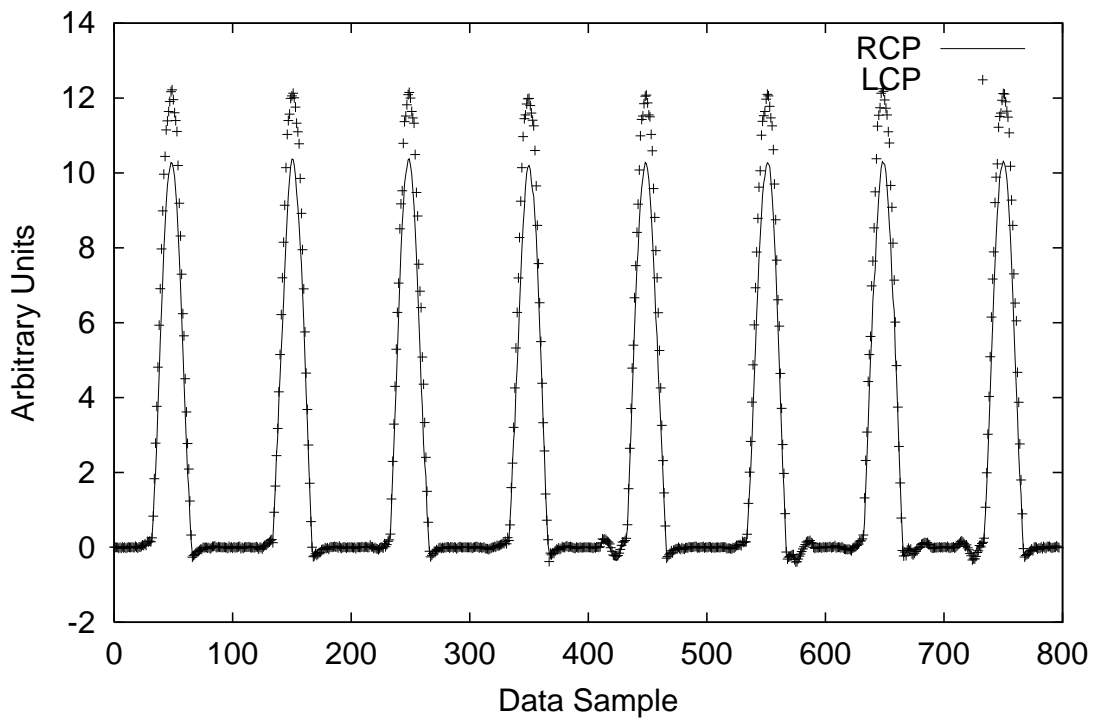


Fig. 10.— X-band beam map of Cas A scanning at 8 different approach angles (every 45°). Samples are taken every $30''$. Power in each polarization is shown in arbitrary units. Hysteresis may be present at the 2% level, with other artifacts (diffraction spikes) in some scans at the 3 – 4% level. No Airy ring structure is evident at $< 1\%$ in amplitude, meaning $< 4\%$ power in the first Airy ring.

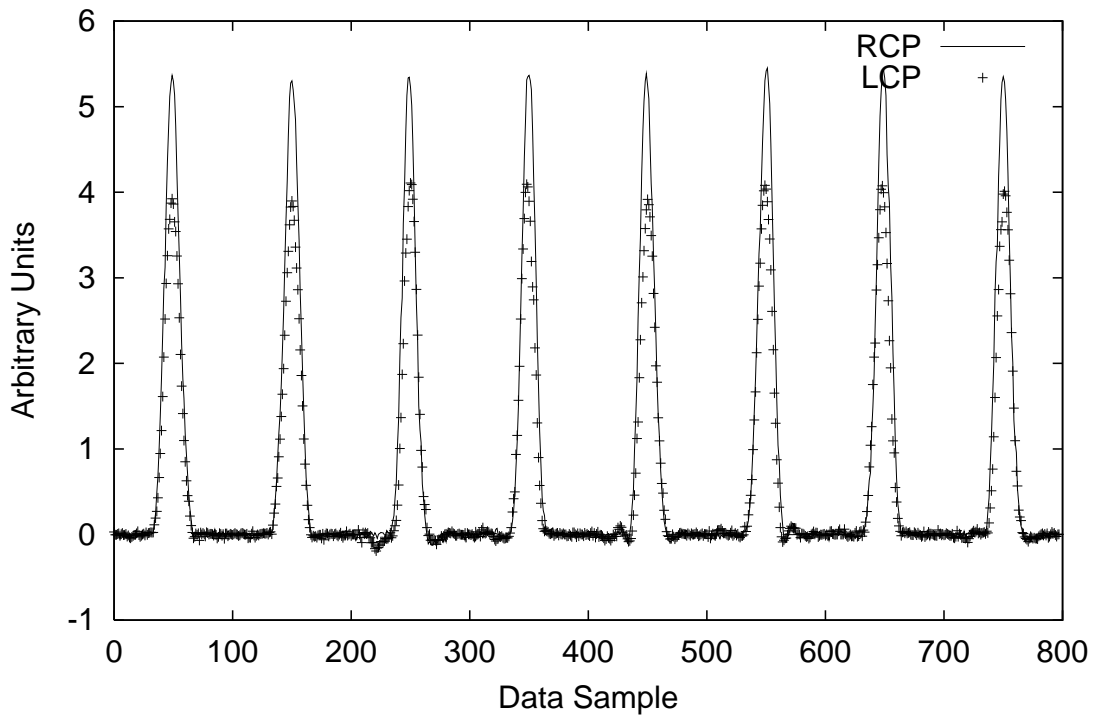


Fig. 11.— Ku-band beam map of Cas A scanning at 8 different approach angles (every 45°). Samples are taken every 30''. Power in each polarization is shown in arbitrary units. The hysteresis seen in X-band is absent, but diffraction spikes ($\pm 3\%$) appear next to peaks 5 and 6 because that scan was slightly off center. A data glitch appears before peak 3 in one polarization. Sidelobes are estimated to be < 1% in amplitude, meaning < 4% power in the first Airy ring.

Table 1. Correlation slope results

ν GHz	Seg 0 $j_\nu/\tau_{100\mu}$	Seg 15 $j_\nu/\tau_{100\mu}$	Seg 30 $j_\nu/\tau_{100\mu}$	Seg 45 $j_\nu/\tau_{100\mu}$	W40 $j_\nu/\tau_{100\mu}$
0.408	18.30 ± 5.60	18.75 ± 5.71	11.80 ± 3.52	13.37 ± 4.23	11.33 ± 5.00
2.326	10.33 ± 1.36	9.81 ± 1.31	7.90 ± 0.96	7.36 ± 1.14	17.68 ± 1.16
8.35	5.37 ± 0.51	5.13 ± 0.57	5.60 ± 0.44	4.67 ± 0.61	12.56 ± 1.18
14.35	5.38 ± 0.99	7.75 ± 1.34	7.95 ± 0.95	7.62 ± 1.05	12.61 ± 1.14
22.5	6.05 ± 0.43	6.65 ± 0.25	6.69 ± 0.23	6.15 ± 0.24	12.59 ± 0.41
32.7	5.24 ± 0.39	5.86 ± 0.21	5.97 ± 0.25	5.19 ± 0.24	12.87 ± 0.39
40.6	4.86 ± 0.36	5.42 ± 0.20	5.53 ± 0.26	4.70 ± 0.23	12.72 ± 0.43
60.7	4.81 ± 0.33	5.35 ± 0.18	5.47 ± 0.23	4.69 ± 0.21	12.37 ± 0.36
93.1	9.20 ± 0.00	9.20 ± 0.00	9.20 ± 0.00	9.20 ± 0.00	16.57 ± 0.00

Note. — Correlation slopes (emission per dust $100\mu\text{m}$ optical depth, $\tau_{100\mu}$) for Haslam (0.408 GHz), Rhodes (2.326 GHz), Green Bank (8.35, 14.35 GHz), and *WMAP* (22.5 – 93.1 GHz) in units of MJy sr^{-1} . To convert to emissivity per H atom ($\text{Jy cm}^2\text{sr}^{-1}$ per H), divide by 2.13×10^{18} . Error values represent the 1σ width of the distribution of slopes as seen in Figure 6, not the (much smaller) uncertainty of the mean. The *WMAP* bands are rather broad; the listed *WMAP* frequencies are effective central frequencies for emission with a free-free spectrum, given by Page *et al.* (2003). The highest frequency *WMAP* band, dominated by thermal dust emission, is used as the “dust template” in this paper, and has no measured error. The W40 spectrum is substantially contaminated by free-free emission at 94 GHz, resulting in a higher normalization (see §5.5 for details). Conversion from *WMAP* thermal dust to $\tau_{100\mu}$ is described in §5.2.